Materials Today Bio 12 (2021) 100147

Contents lists available at ScienceDirect

Materials Today Bio

journal homepage: www.journals.elsevier.com/materials-today-bio

Biofunctional magnesium-coated Ti6Al4V scaffolds promote autophagy-dependent apoptosis in osteosarcoma by activating the AMPK/mTOR/ULK1 signaling pathway

X. Wei [a,e], Z. Tang [a,e], H. Wu [a,e], X. Zuo [a], H. Dong [a], L. Tan [b], W. Wang [c], Y. Liu [a], Z. Wu [a], L. Shi [a], N. Wang [a], X. Li [d,***], X. Xiao [a,**], Z. Guo [d,*]

[a] Department of Orthopaedics, Xijing Hospital, Fourth Military Medical University, Xi'an, Shaanxi, 710032, PR China
[b] Institute of Metal Research, Chinese Academy of Science, Shenyang, 110016, PR China
[c] Department of Immunology, State Key Laboratory of Cancer Biology, Fourth Military Medical University, Xi'an, Shaanxi, 710032, PR China
[d] Department of Orthopaedics, Tangdu Hospital, Fourth Military Medical University, Xi'an, Shaanxi, 710038, PR China

ARTICLE INFO

Keywords:
Magnesium
Coating
Antitumour
Autophagy
Apoptosis

ABSTRACT

The recurrence of osteosarcoma (OS) after reconstruction using Ti6Al4V prostheses remains a major problem in the surgical treatment of OS. Modification of the surfaces of Ti6Al4V prostheses with antitumor functions is an important strategy for improving therapeutic outcomes. Magnesium (Mg) coating has been shown to be multifunctional: it exhibits osteogenic and angiogenic properties and the potential to inhibit OS. In this study, we determined the proper concentration of released Mg^{2+} with respect to OS inhibition and biosafety and evaluated the anti-OS effects of Mg-coated Ti6Al4V scaffolds. We found that the release of Mg^{2+} during short-term and long-term degradation could significantly inhibit the proliferation and migration of HOS and 143B cells. Increased cell apoptosis and excessive autophagy were also observed, and further evidence of AMPK/mTOR/ULK1 signaling pathway activation was obtained both *in vitro* and *in vivo*, which suggested that the biofunctional scaffolds induce OS inhibition. Our study demonstrates the ability of an Mg coating to inhibit OS and may contribute to the further application of Mg-coated Ti6Al4V prostheses.

1. Introduction

Osteosarcoma (OS), the most common primary malignant tumor of bone among children and adolescents, exhibits a high degree of malignancy and a high rate of recurrence [1]. Reconstruction using titanium alloy (Ti6Al4V) prostheses after limb-salvage treatment is the main surgical therapy for OS [2]. However, the high rate of local recurrence, which is 30%–40% within 3 years after treatment, remains a major problem experienced by orthopedic oncologists, and the causes of OS recurrence remain unknown [3,4]. Recent studies have shown that a considerable factor involved in recurrence is the long-term *in vivo* implantation of Ti6Al4V prostheses [5,6]. The ions (titanium, aluminum, and vanadium) and particulate fragments released during implantation react with the surrounding normal tissue to induce chronic inflammation around the prostheses over time. This continuous microenvironment can promote the reproliferation of OS cells in the cancerous area around the prosthesis, which, in turn, increases the risk of tumor recurrence [7].

Magnesium (Mg) is considered a revolutionary bioactive metal due to its degradability and the multiple biological functions of its degradation products [8]. Many studies have shown that Mg degradation products are not cytotoxic, do not induce a foreign body reaction, and are essential elements for the human body [9–11]. In recent years, Mg^{2+} ions produced during degradation have also been found to inhibit the growth of tumor cells. Studies have shown the clear inhibitory effect of Mg on breast cancer [12] and ovarian tumors [13], and Mg can inhibit the proliferation and promote the apoptosis of OS cells [14–16]. Although the tumor-inhibiting effect of Mg^{2+} ions has been verified, the specific mechanisms remain not well understood. The antitumor effect of Mg is

* Corresponding author.
** Corresponding author.
*** Corresponding author.
E-mail addresses: lxkfmmu@163.com (X. Li), xiao_xxtyfsxx@sina.com (X. Xiao), guozheng@fmmu.edu.cn (Z. Guo).
[e] These authors have contributed equally to this study.

https://doi.org/10.1016/j.mtbio.2021.100147
Received 23 August 2021; Received in revised form 30 September 2021; Accepted 5 October 2021
Available online 12 October 2021

related to the local concentration of released Mg^{2+} ions. Although the excessive release of Mg^{2+} ions can inhibit tumor cells, normal cells, including mesenchymal stromal cells (MSCs), and endothelial progenitor cells (EPCs), can also be effectively suppressed [17]. The proper concentration of released Mg^{2+} ions should be carefully defined and controlled prior to application, and the application of Mg-based prostheses is limited by rapid corrosion and insufficient mechanical strength [10].

Considering the outstanding bioactivity of Mg and the strong mechanical strength of Ti6Al4V, some recent studies have effectively combined these two metallic materials to generate composites [18,19]. In our previous study, a Mg coating was successfully deposited on the surface of Ti6Al4V scaffolds, and the coated scaffolds significantly promoted angiogenesis and osteogenesis *in vitro* and *in vivo* [20,21]. Further investigations indicated that the Mg coating could also inhibit OS; hence, Mg-coated Ti6Al4V prostheses may reduce the probability of OS recurrence after implantation. However, the molecular mechanism has not been defined, which restricts the further application of Mg-coated Ti6Al4V prostheses against OS. Variations in the concentration of sustainably released Mg^{2+} ions may exert multiple effects on the metabolism and proliferation of OS cells, which is a crucial problem for the clinical use of biodegradable materials.

A growing number of studies have shown that autophagy induction can promote OS cell death [22–24]. Basal autophagy can help cells adapt to various adverse environments, but excessive autophagy activates programmed cell death, termed 'autophagy-dependent apoptosis' [25,26]. Additionally, many metal cations are closely related to cellular autophagy [27]. Potassium ions [28], ferric ions [29], copper ions [30], and zinc ions [31] can promote autophagy-dependent apoptosis in tumor cells through different mechanisms. Because Mg is a ubiquitous element in organisms, the local aggregation of Mg ions may also impact the progression of autophagy and subsequently trigger apoptosis in OS cells. Specific studies aiming to determine whether Mg^{2+} ions can trigger autophagy and the signaling pathways through which this effect is induced are needed.

In this study, we defined the optimal Mg^{2+} concentration for inhibiting four OS cell lines (HOS, 143B, SAOS2, and U2OS). We then designed modified Mg-coated Ti6Al4V scaffolds to achieve the proper release of Mg^{2+} ions and investigated the anti-OS effects of the scaffolds *in vitro* and *in vivo*. To further elucidate the specific mechanism through which the Mg coating exerts its antitumor effect, we also explored whether Mg^{2+} ions affect apoptosis by promoting autophagy in OS cells and the specific signaling pathways activated during this process. Through the present study, we hope to fully investigate the properties of Mg-coated Ti6Al4V scaffolds and provide a better prosthetic manufacturing solution for postoperative reconstruction following OS in the future.

2. Methods

2.1. Mg coating deposition on porous Ti6Al4V scaffolds

Porous Ti6Al4V scaffolds were manufactured by electron beam melting (EBM) 3D printing. Briefly, an STL model of the scaffolds was transferred into an EBM machine. A thin layer of medical-grade Ti6Al4V powder was preheated to 650 °C to generate a cross-section layer by electron beam scanning under vacuum conditions (10^{-4}–10^{-5} mbar). This progress was repeated layer by layer until completion. The fabricated Ti6Al4V scaffolds exhibited 68 ± 5% porosity with a pore size of 710 ± 42 μm.

Mg coatings were deposited on 3D-printed porous Ti6Al4V scaffolds by multiarc ion plating using manufacturing procedures according to our previous research [20]. In brief, the surface of porous Ti6Al4V scaffolds was used to bombarded and sputtered with highly pure Mg (99.99%). During this process, the constant target arc current was 50 A, with $P_{Ar} = 3.5 \times 10\text{-}2$ Pa for 5 min. The current density used in the negative bias voltage application was in the range of 0.12–0.16 A. During deposition, a pulsed power source superimposed a negative pulse bias to the substrates (pulse bias magnitude Up = 100 V, pulse frequency f = 30 kHz, and duty ratio D = 40%). A constant two-arc source current of 0.1 A was maintained. During deposition, the distance between Ti6Al4V samples and the cathode arc target was 400 mm, and the total deposition time was 60 min. The sputtering temperature of the titanium alloy was maintained at 235 °C.

2.2. Mg^{2+} release and pH testing

The samples were immersed in D-Hank's solution (Mg^{2+} free) for 30 days at 37 ± 0.5 °C with an immersion ratio of 0.2 g/mL to obtain Mg-coated Ti6Al4V scaffolds according to ISO 10993–12. Every 3 days (every day for the first 6 days), the solutions were refreshed to simulate *in vivo* conditions. Each time the extracts were collected, the pH value was tested and recorded, and the released Mg^{2+} ions were estimated by inductively coupled plasma-optical emission spectrometry (ICP-OES, ICAP7400, Thermo Scientific). All the tests were repeated in triplicate for each group and at each time point.

2.3. Surface characterization

The surface morphology of the Mg-coated surface was detected after 0, 3, 6, and 21 days of Mg^{2+} release by scanning electron microscopy (SEM) (S-4800, Hitachi), and the composition of the coating was analyzed by energy-dispersive X-ray spectroscopy (EDS). For improving the electrical conductivity of the materials, the Mg-coated Ti6Al4V scaffolds were fixed on trays with a conductive adhesive, and Pt was sprayed on both sides of the samples using an E−1010 ion sputter coater (SuPro Instruments).

2.4. Cell culture

The human OS cell lines HOS, 143B, SAOS2, and U2OS, which were purchased from the China Center for Type Culture Collection, were cultured in Dulbecco's modified Eagle medium (DMEM, HyClone) supplemented with 10% fetal bovine serum (FBS, IC-1900, InCellGene LLC.) and 1% penicillin-streptomycin under conditions of 95% humidity, 5% CO_2 and a constant temperature of 37 °C.

2.5. Mg concentrations used for OS cell culture

The basal Mg^{2+} concentration in complete DMEM was 0.8 mM. The medium was supplemented with sterile $MgCl_2$ was used to obtain conditional complete DMEM with an Mg^{2+} concentration of 5 mM, 10 mM, 15 mM, and 20 mM.

2.6. Preparation of the coculture system for in vitro experiments

Coculture experiments were conducted using Transwell chambers (pore size, 0.4 μm; Corning). After sterilization by exposure to Co^{60} radiation for 72 h, the scaffolds were set in the upper chamber of the coculture system and immersed in pure complete DMEM (pM) according to ISO 10993–12 (Fig. 3A). Before seeding OS cells in the bottom, the Ti6Al4V scaffolds were incubated under cell culture conditions for 30 days (denoted 'Ti'), and the Mg-coated Ti6Al4V scaffolds were incubated for 3 days and 30 days (denoted 'MgA' and 'MgB,' respectively).

2.7. Assessments of cytotoxicity and cell proliferation

OS cells were seeded on 96 plates at a density of 1×10^3 per well and cultured in conditional complete DMEM for 1–5 days. At 0 h and 1.5 h after the addition of 10% CCK-8 reagent from a kit (Dojindo), the absorbance at 450 nm (Ab450) was measured using a microplate reader (Biotek Synergy H1). For the assessment of cell proliferation and cytotoxicity under different conditions, the cell viability was calculated using

the following formula:

$$\Delta \mathrm{Ab450} = Ab450\ at\ 1.5\ h - Ab450\ at\ 0\ h$$

$$cell\ viability = \frac{\Delta Ab450\ of\ experimental\ group}{\Delta Ab450\ of\ control}$$

After 48 h of coculture, cytotoxicity was investigated by live/dead assays. Briefly, the same volume of CytoCalcein™ Green/Propidium Iodide dye-work solution from the Live or Dead™ Cell Viability Assay Kit (AAT Bioquest) was added to each well. The cells were then incubated at 37 °C for 1 h and washed with phosphate buffered saline (PBS), and the green/red dual fluorescence was then captured by fluorescence microscopy (Axio Observer, Carl Zeiss).

2.8. Cell apoptosis

The apoptosis rates of OS cells in different groups were analyzed after 48 h of coculture. Annexin V-FITC/propidium iodide (PI) double staining and flow cytometry were used for the detection of apoptotic cells. Briefly, 1×10^6 cells from each sample were resuspended in 1 mL of complete medium containing Annexin V-FITC (50 μL). After 10 min of incubation in the dark, binding buffer (1.5 mL) and PI (15 μL) were added. The samples were immediately assessed by flow cytometry (FACS Vantage SE, BD Biosciences). The enzyme activity of caspase-3 in the cell lysates was detected by a spectrophotometric assay (Solarbio). Briefly, the cocultured cells in the different groups were collected and washed with PBS. After the addition of 150 μL of cell lysis buffer and incubation for 15 min on ice, the cell lysate was centrifuged, and the supernatant was collected. Subsequently, 50 μL of the sample solutions was mixed with 40 μL of buffer and 10 μL of Ac-DEVD-pNA (2 mM) to form a 100-μL reaction system. The absorbance of the samples and blank control at 405 nm (A405) were measured. pNA in the samples was then calculated by comparing the ΔA405 values with the pNA standard curve. A One-Step TUNEL (terminal deoxynucleotidyl transferase (TdT)-mediated dUTP nick end-labeling) fluorescent kit (Beyotime) was also used for the detection of apoptotic cells. After permeabilization with 0.1% Triton X-100, the cocultured cells were stained with a fluorescein isothiocyanate (FITC)-labeled TUNEL Kit for 1 h at 37 °C. The TUNEL-positive cells were then captured by fluorescence microscopy (Axio Observer, Carl Zeiss).

2.9. Plate cloning assay

Single-cell suspensions were prepared by collecting cells from each group at the logarithmic phase of growth. Each group of cells was seeded at a density of 200 cells per dish, and the dishes were gently shaken to evenly disperse the cells. After coculture of the cells belonging to the different groups for 14 days, the dishes were washed twice with PBS, and the cells were then fixed with 4% paraformaldehyde for 15 min and subjected to crystal violet staining to observe and count the clones.

2.10. Cell immigration and invasion assays

Wound healing and Transwell assays were performed for the evaluation of cell migration and invasion, respectively. Briefly, when the density of the cocultured OS cells reached 90–95%, a straight line through the middle of the cells was scratched in each well. After 0 or 24 h, images were collected using an inverted microscope, and the distance between the two edges of each wound was calculated using Image-Pro Plus 6 software. For the Transwell assays, the positions of the OS cells and scaffolds in the coculture system were swapped. The OS cells were resuspended in serum-free DMEM and seeded in Matrigel-coated Transwell chambers (pore size, 8 μm; Corning) at a density of 1×10^5/mL, whereas the scaffolds were preincubated at the bottom. After coculture for 24 h, the cells inside the Transwell chambers were removed with a cotton swab, and the cells that had migrated outside were fixed with 4% paraformaldehyde, stained with 0.5% crystal violet, and observed by light microscopy (Cx21, Olympus, Japan).

2.11. Immunofluorescence (IF) analysis of LC3

After coculture for 48 h, HOS and 143B cells were fixed in 4% paraformaldehyde and then incubated with primary antibody against LC3 (microtubule-associated protein 1A/1B-light chain 3, Proteintech, 14600-1-AP) overnight at 4 °C and then with a fluorescent secondary antibody (Abbkine, A23420) for 1 h. Images of LC3 puncta were captured by fluorescence microscopy (Axio Observer, Carl Zeiss) under laser excitation, and the number of puncta were counted using Image-Pro Plus 6 software.

2.12. Autophagic flux detection

The autophagic flux in the cells was tracked using mCherry-GFP-labeled LC3 (Hanbio Biotechnology, AP20101508) as previously reported [32]. The 143B and HOS cells were transfected with mCherry-GFP-LC3 adenovirus for 6 h and then cocultured in different groups for 48 h mCherry-GFP-LC3 expression and tracked and captured by fluorescence microscopy under laser excitation. The mCherry and GFP dots were then counted using Image-Pro Plus 6 software.

2.13. TEM images of autophagosomes

143B and HOS cells were cocultured in the different groups and collected after 48 h. The samples were then fixed with glutaric dialdehyde and osmic acid. The samples were dehydrated with an ethanol gradient and dried with propylene oxide to prepare ultrathin sections. Images of the sections of fixed cells were then captured by transmission electron microscopy (TEM, JEM-1400Flash) at a magnification of 10,000×.

2.14. Western blot assay

Cocultured OS cells belonging to the different groups were lysed with radioimmune precipitation assay (RIPA) buffer and centrifuged at 12,000 RPM (revolutions per minute) for protein collection. Total protein was quantified with a BCA Protein Assay Kit (Thermo Scientific, 23,227). Each sample was then loaded on 8–12% SDS-PAGE gels to separate the proteins, and the proteins were transferred to a PVDF membrane. The membrane was incubated with primary antibodies overnight and a secondary antibody for 1 h (Supplementary 1). An ultrasensitive luminescent solution was then used for the detection of the proteins on the membrane. The greyscale values from the Western blot images were analyzed using ImageJ 1.52v software.

2.15. Inhibition of autophagy-related apoptosis

Chloroquine (CQ, Sigma, C6628) and 3-methyladenine (3-MA, Sigma, M9281) were used to inhibit autophagy in 143B and HOS cells cocultured with the samples, respectively. The concentration of CQ in the culture medium was 20 μM, and the concentration of 3-MA was 10 mM. IF staining of LC3 (described in section 2.11), autophagic flux detection (described in section 2.12), and TEM (described in 2.13) were performed to confirm the inhibition of autophagy. The cell apoptosis rates in the control and autophagy-inhibited groups were then measured by flow cytometry as described in section 2.8.

2.16. Detection of the AMPK-mTOR-ULK-1 pathway

The AMPK (adenosine 5′-monophosphate (AMP)-activated protein kinase), mTOR (mammalian target of rapamycin), and ULK1 (unc-51 like autophagy activating kinase 1) proteins and their phosphorylation in the different groups were detected by Western blot analysis. Compound C

(10 μM, MCE, HY13418) was added to the coculture system to inhibit AMPK. The expression of downstream proteins was then detected by Western blot analysis, and IF staining of LC3 was performed to assess autophagy as described in section 2.11.

2.17. Verification of anti-OS activity in vivo

Twelve six-to eight-week-old nude (nu/nu) mice were purchased from the FMMU Experimental Animal Center. All experimental procedures were approved by the Ethics Committee of FMMU. A cell suspension containing 2×10^6 143B cells was subcutaneously injected into the backs of the nude mice to establish OS model mice. When the diameters of the tumors reached approximately 3 mm, the extracts from each group were injected into the subcutaneous tissue in the vicinity of the tumorigenic site every three days to simulate the degradation of bioactive scaffolds near sites of OS *in vivo*. The extracts of the samples were previously collected as described in section 2.2. 'Ti' denotes the extracts of Ti6Al4V scaffolds at 30 days; 'MgA' and 'MgB' denote the extracts of Mg-coated Ti6Al4V scaffolds at 3 days and 30 days; D-Hank's solution was used as a control. Before each injection and until 30 days after the first injection, the length (L) and width (W) of the tumor were measured and recorded. The volumes (V) of the tumors were then calculated using the formula $V = LW^2$. After anesthesia, the tumor-bearing mice were sacrificed, and the intact tumors were collected and used for IF and TUNEL staining for the analysis of apoptosis. Briefly, the tumors were dehydrated with an ethanol gradient and embedded in paraffin. Subsequently, 5-μm-thick sections were prepared, and tumor inhibition was evaluated by IF staining and TUNEL apoptosis staining. The sections were also subjected to hematoxylin-eosin (HE) staining to observe the histopathologic differences between groups.

2.18. Statistical analysis

All statistical results were analyzed using GraphPad Prism software version 8.2 (GraphPad, San Diego, US). The student's t-test was used to

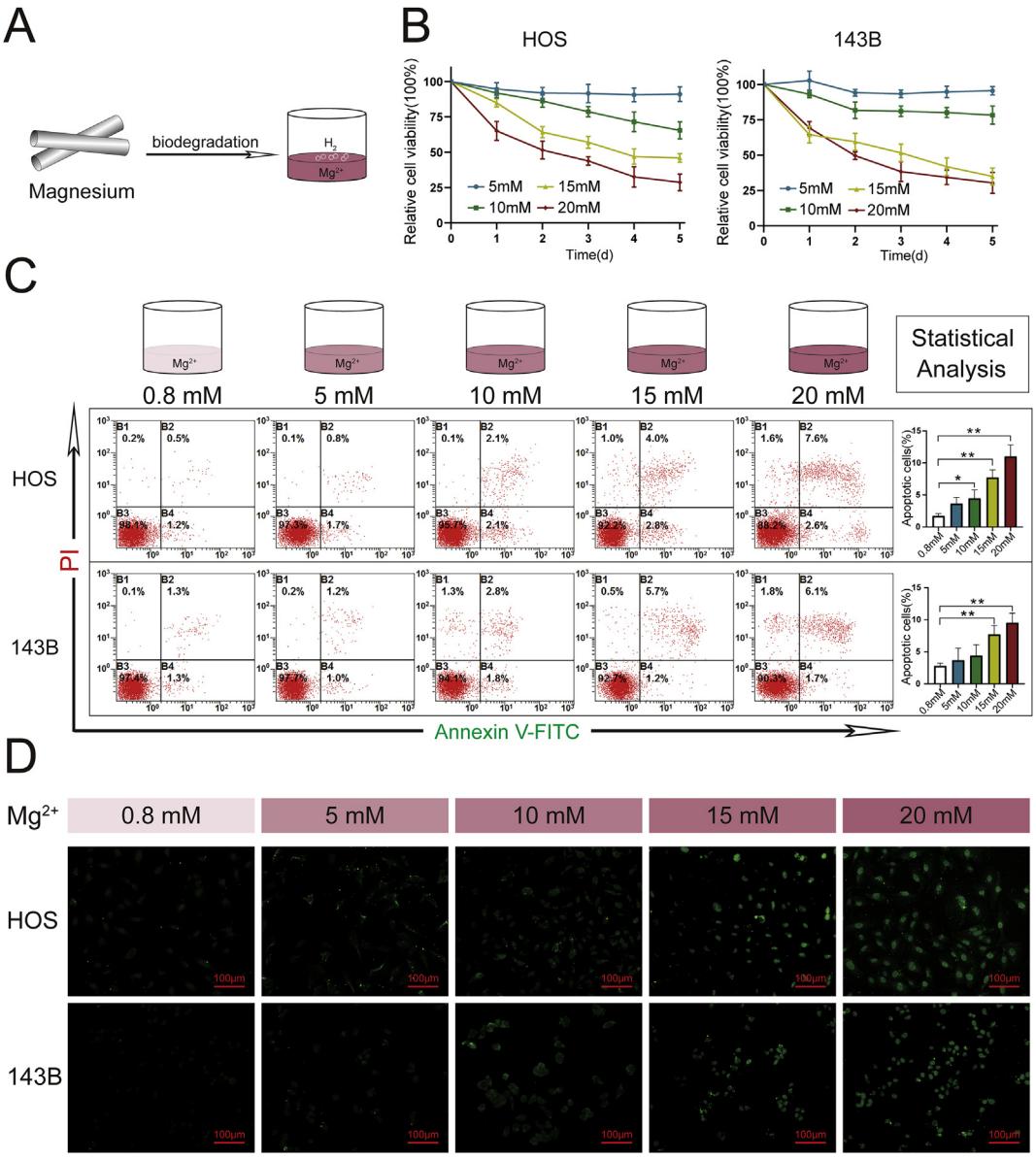

Fig. 1. Effects of Mg^{2+} release on the viability and apoptosis of OS cells. **(A)** Mg^{2+} release during the biodegradation of Mg metal. **(B)** Viabilities of HOS and 143B cells cultured in conditioned medium containing different concentrations of Mg^{2+} ions. **(C)** Apoptosis rates of HOS and 143B cells were analyzed by flow cytometry following Annexin V-PE/PI staining. n = 3; *p < 0.05; **p < 0.01. **(D)** TUNEL staining of HOS and 143B cells. TUNEL-positive cells are stained green.

compare two groups, and one-way analysis of variance (ANOVA) was used for the statistical analysis of multiple comparisons with *Tukey's post hoc* test. All statistical values obtained in this study are shown as the means ± standard errors of the measurements (SEMs). A difference was considered statistically significant if p-value < 0.05 (*$p < 0.05$ and **$p < 0.01$).

3. Results

3.1. Mg^{2+} at appropriate concentrations could effectively inhibit OS cell viability and promote OS cell apoptosis

The viability and apoptosis rates of 143B and HOS cells cultured with 0.8 mM (control), 5 mM, 10 mM, 15 mM, or 20 mM Mg^{2+} are shown in Fig. 1. In the presence of an Mg^{2+} concentration higher than (or equal to) 10 mM, the viability of the OS cells decreased with increases in the culture time. In addition, OS cells were more effectively inhibited by treatment with Mg^{2+} at relatively high concentrations (15 mM and 20 mM). The numbers of apoptotic OS cells detected by flow cytometry and TUNEL staining were also clearly in the groups treated with 15 mM and 20 mM Mg^{2+}. Similar trends of cell viability and apoptosis were also observed with the other OS cell lines (SAOS2 and U2OS, Supplementary 2).

3.2. Characteristics of the biofunctional Ti6Al4V scaffolds and progressive Mg^{2+} release curves

Before degradation, the Mg coating showed a uniform granular shape, and elemental analysis showed that Mg was the dominant element (Fig. 2A). After degradation for 3 days, the granular structure at the surface exhibited fine pores and cracks. After 6 days of degradation, a relatively tight structure and more obvious cracks were observed on the surface of the Ti6Al4V scaffolds. After approximately 3 weeks (21 days) of degradation, the surface of the Ti6Al4V scaffolds exhibited larger coating particles with large cracks on the surface of the particles (Fig. 2B). The Mg^{2+} release curve showed that a relatively high and sustained concentration of Mg^{2+} (20–25 mM) could be rapidly obtained from the scaffolds. Although the pH value increased with the rapid release of Mg^{2+} at the early stage of degradation, this value soon stabilized to the same level observed with the Ti6Al4V scaffolds (Fig. 2C).

3.3. The Mg-coated Ti6Al4V scaffolds suppressed the proliferation and invasion of OS cells

OS cells were cocultured with preincubated scaffolds, as shown in Fig. 3A. The proliferation of 143B and HOS cells in the MgA and MgB groups was significantly lower than that of the cells in the pM and Ti

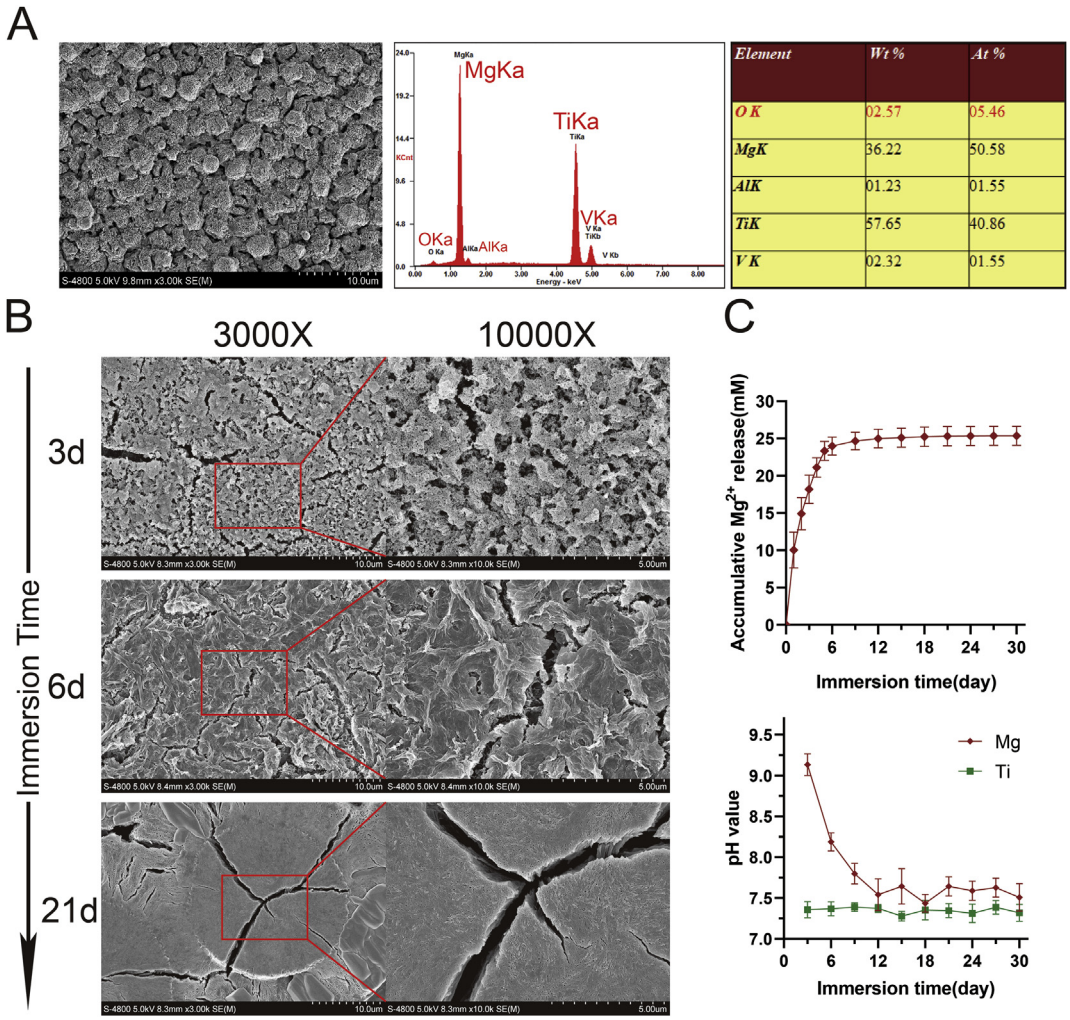

Fig. 2. Progressive Mg^{2+} release during surface degradation of the Mg-coated Ti6Al4V scaffolds. (**A**) Surface morphology was examined by SEM (3000x), and the elemental composition of the Mg-coated Ti6Al4V scaffolds before degradation was analyzed by EDS. (**B**) The different surface morphologies of Mg-coated Ti6Al4V scaffolds during immersion were examined by SEM. (**C**) Mg^{2+} release and variations in pH after immersion of the Mg-coated Ti6Al4V scaffolds.

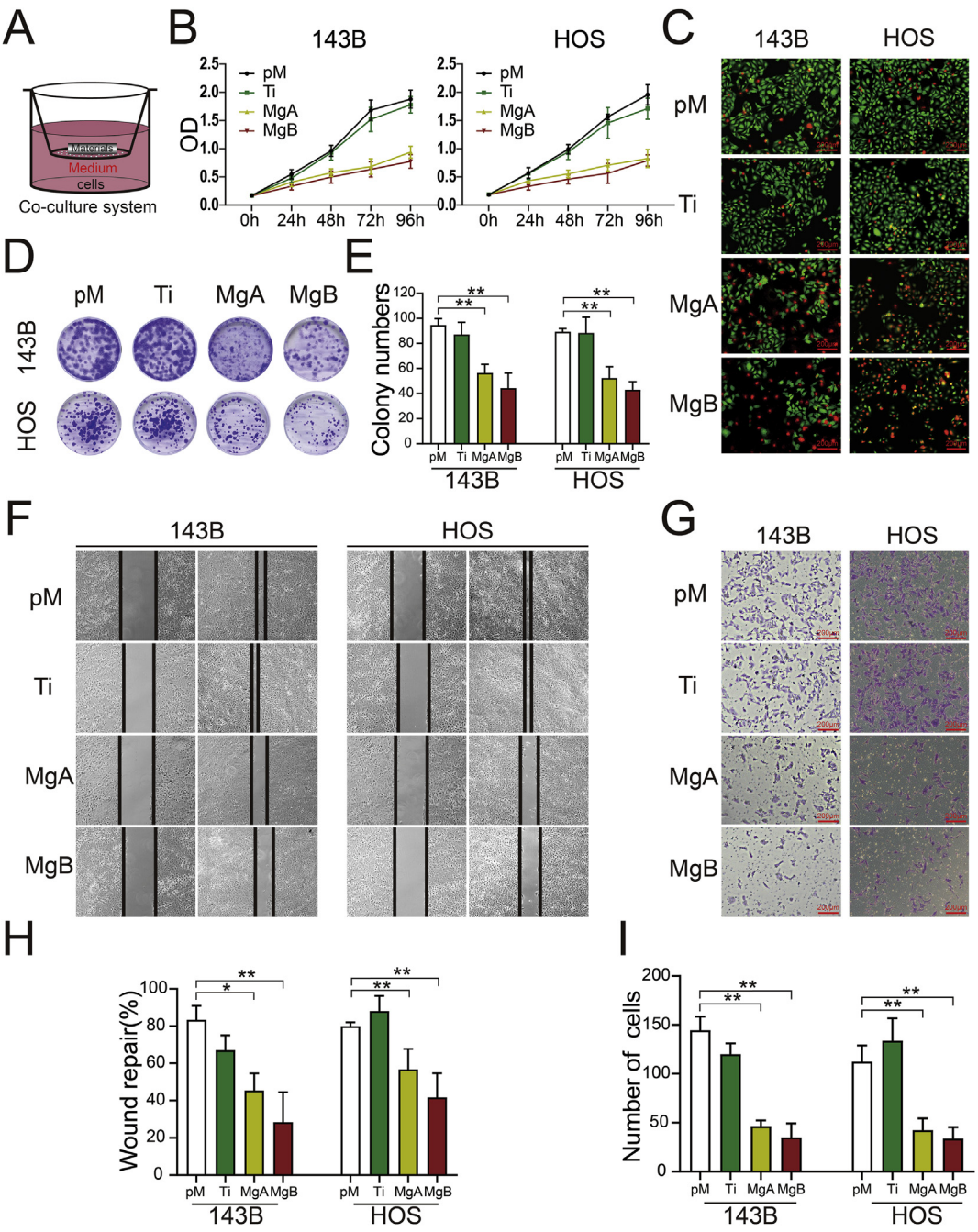

Fig. 3. Effects of the Mg-coated Ti6Al4V scaffolds on the proliferation, migration, and invasion of 143B and HOS cells. (**A**) Schematic diagram showing OS cell coculture with the scaffolds. (**B**) CCK-8 assay analysis of 143B and HOS cell proliferation after 0, 24, 48, 72, and 96 h. (**C**) Live/dead viabilities of 143B and HOS cells cocultured for 48 h (live cells are stained green, and dead cells are stained red). (**D**) Images and (**E**) colony numbers were obtained from the plate cloning assay after 14 days. n = 3; **p < 0.01. (**F**) Images of wound healing and (**G**) invasion assays with 143B and HOS cells cocultured in the different groups. (**H**) The rates of wound repair and (**I**) numbers of migrated cells were analyzed. n = 3; *p < 0.05; **p < 0.01.

groups, as shown in Fig. 3B. Furthermore, the live/dead staining results shown in Fig. 3C indicated that increased levels of 143B and HOS cell death in the MgA and MgB groups. The results from the plate cloning experiments are shown in Fig. 3D and E; for the two OS cell lines, fewer clones were obtained in the MgA and MgB groups than in the pM and Ti groups after 14 days of coculture. The results from the wound healing and Transwell assays are shown in Fig. 3F and G. After 24 h of coculture, the scratches in the MgA and MgB groups of the two OS cell lines were significantly wider than those in the pM and Ti groups, and the differences between the Ti and pM groups were not significant (Fig. 3H). Compared with the results found for the pM and Ti groups, fewer cells in the MgA and MgB groups passed through the Transwell membrane into the lower layer, and the differences between the Ti and pM groups were not significant (Fig. 3I).

3.4. *The Mg-coated Ti6Al4V scaffolds increased OS cell apoptosis*

As shown in Fig. 4A and B, the percentages of apoptotic cells in the MgA and MgB groups were significantly higher than those in the pM group, but no significant difference was found between the Ti and pM groups. Additionally, after 48 h of coculture, the caspase-3 enzyme

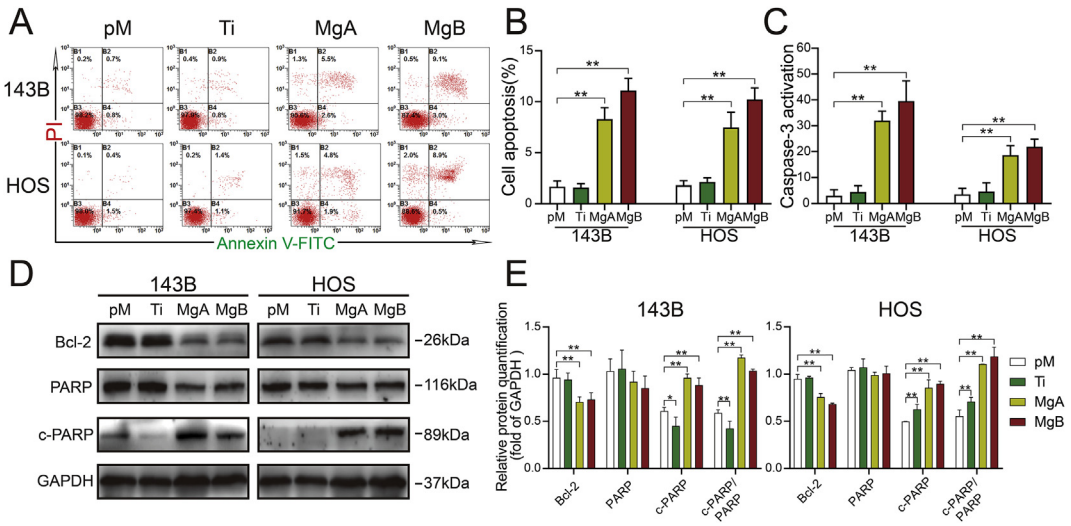

Fig. 4. The Mg-coated Ti6Al4V scaffolds increased the apoptosis of 143B and HOS cells. (**A**) Results from the flow cytometric analysis of cell apoptosis following Annexin V-PE/PI staining. (**B**) The proportions of apoptotic cells were determined. n = 3; **p < 0.01. (**C**) Caspase-3 activity in 143B and HOS cells was detected after 48 h n = 3; **p < 0.01. (**D**) Western blot analysis of Bcl-2, PARP, and cleaved PARP levels in 143B and HOS cells after 48 h. (**E**) The relative expression levels were examined by greyscale analysis. n = 3; *p < 0.05; **p < 0.01.

activities in the MgA and MgB groups were significantly higher than those in the pM and Ti groups (Fig. 4C), and this finding was obtained for both OS cell lines. The Western blot analysis (Fig. 4D and E) showed that Bcl-2 expression was decreased in the MgA and MgB groups compared with the pM group, and the ratios of cleaved PARP to PARP were increased in the former groups. The Bcl-2 and cleaved PARP expression levels in the Ti and pM groups of HOS and 143B cells were the same.

3.5. The Mg-coated Ti6Al4V scaffolds enhanced autophagy in apoptotic cells

The results from the IF staining of LC3B in HOS and 143B cells are shown in Fig. 5A. The number of red puncta in the figure indicates the levels of LC3 protein aggregation and activation. More red puncta were clearly observed in the MgA and MgB groups than in the pM and Ti

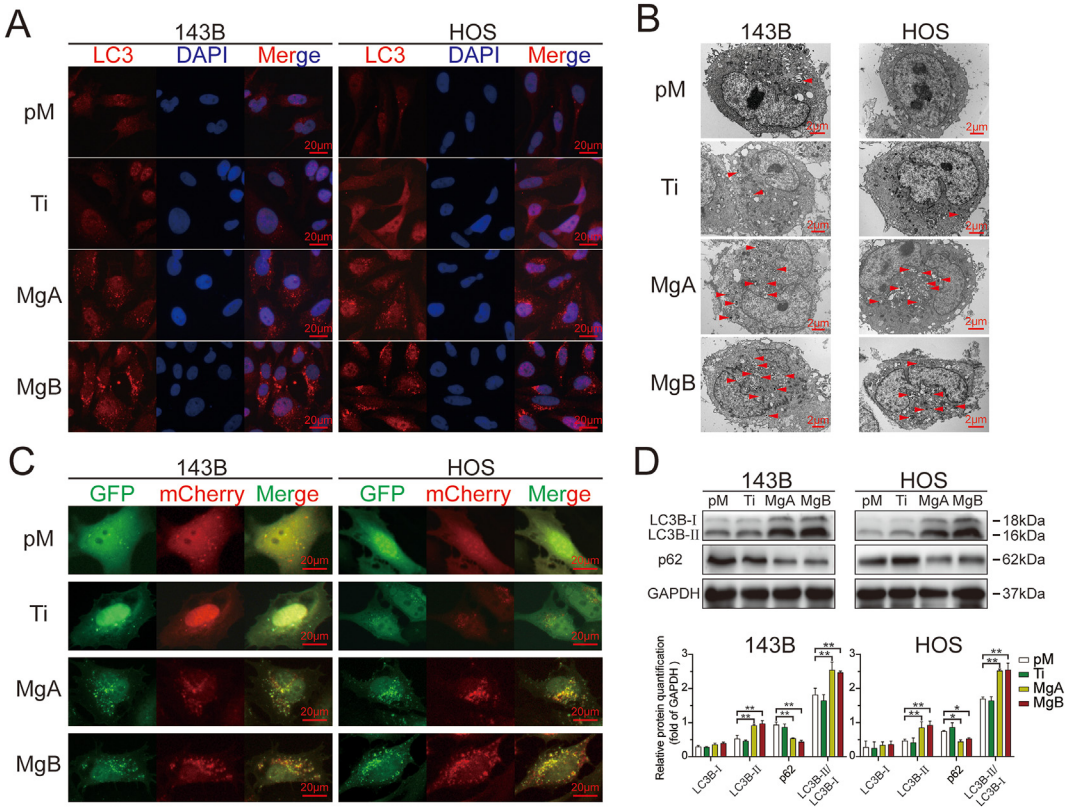

Fig. 5. The Mg-coated Ti6Al4V scaffolds induced an increased level of autophagy in apoptotic 143B and HOS cells. (**A**) Fluorescent inverted microscopy analysis of LC3 puncta in 143B and HOS cells cocultured for 48 h (red; the cells were counterstained with DAPI to show nuclei in blue). (**B**) Transmission electron microscopy of autophagosomes in 143B and HOS cells. (**C**) Fluorescent inverted microscopy of GFP-mCherry-LC3 adenovirus-transfected 143B and HOS cells after 48 h. (**D**) The relative LC3B and p62 expression levels were detected by Western blot analysis and determined by greyscale analysis. n = 3; *p < 0.05; **p < 0.01.

groups (Supplementary 3A). The TEM results also showed that the MgA and MgB groups exhibited more autophagic vesicles with a bilayer membrane structure than the pM or Ti group (Fig. 5B, red triangles, Supplementary 3C). The autophagic fluxes in the different groups of HOS and 143B cells are shown in Fig. 5C. Red mCherry signals and green GFP signals were captured in different channels, and the two channels were fused to show the distributions of autophagosomes (yellow dots in the merged images) and autophagolysosomes (red dots in the merged images). In the pM and Ti groups, few yellow or red dots were observed, which indicated a low level of autophagy. In the MgA and MgB groups, aggregated yellow and red fluorescent dots were observed in the merged images (Supplementary 3B). After 48 h, a Western blot analysis (Fig. 5D) showed that the expression of LC3B-II and the ratio of LC3B-II to LC3B-I were significantly higher in the MgA and MgB groups than in the pM and Ti groups.

3.6. The inhibition of autophagy attenuated OS cell apoptosis induced by the Mg-coated Ti6Al4V scaffolds

The autophagy inhibitors 3-MA and CQ were used to inhibit autophagy. The results from the LC3 IF staining of cocultured HOS cells and 143B cells after autophagy inhibition are shown in Fig. 6A. No significant difference in

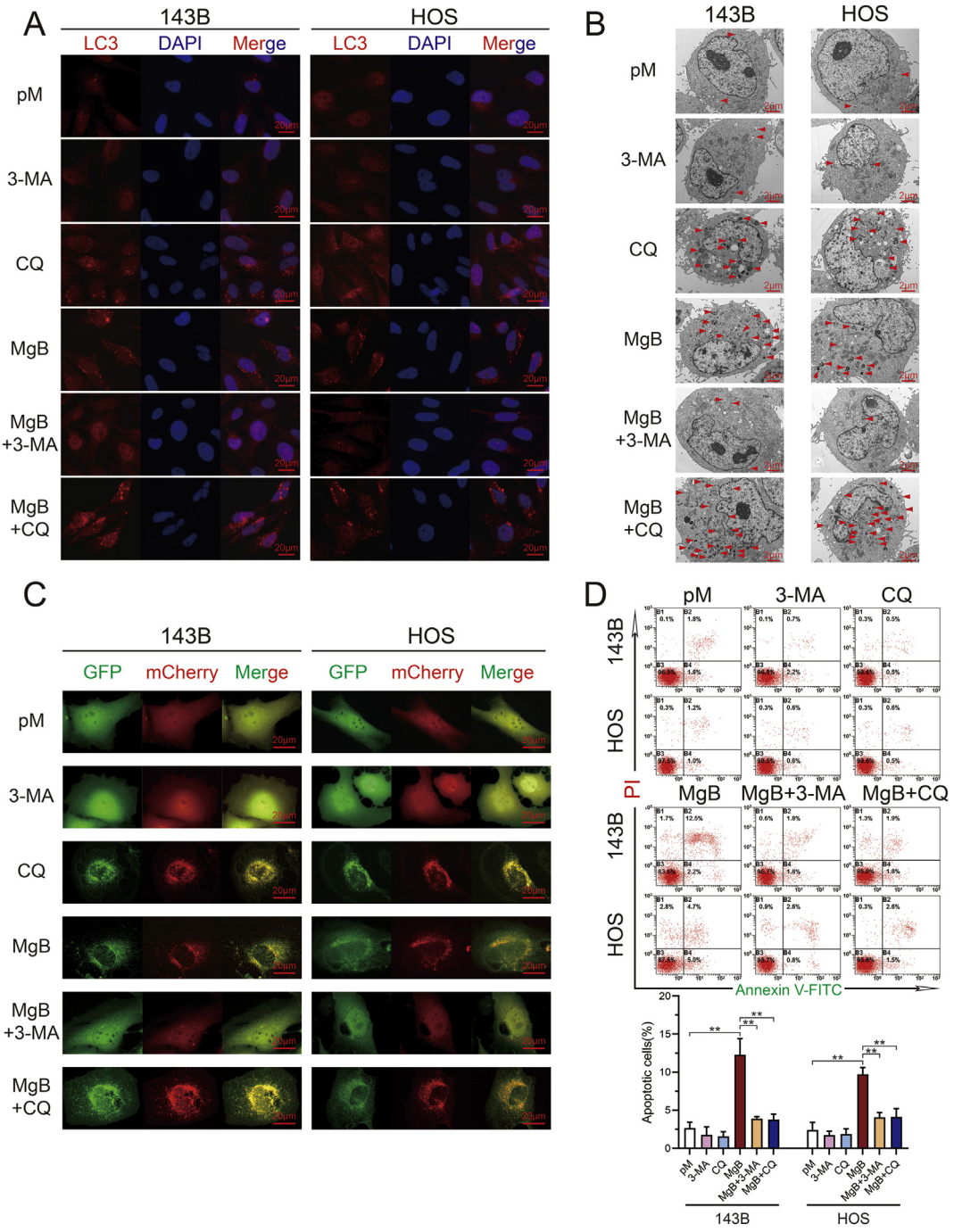

Fig. 6. The inhibition of autophagy alleviated 143B and HOS cell apoptosis induced by the Mg-coated Ti6Al4V scaffolds. (**A**) 143B and HOS cells were cocultured with the Mg-coated Ti6Al4V scaffolds (MgB) in the presence or absence of 10 mM 3-MA or 20 μM CQ; pM and inhibitor groups without scaffolds were established as controls. LC3 puncta formation was captured by fluorescence inverted microscopy. (**B**) TEM images of autophagosomes in 143B and HOS cells. (**C**) Autophagic flux detection in 143B and HOS cells. (**D**) Flow cytometry analysis of 143B and HOS cell apoptosis after coculture. n = 3; *p < 0.05; **p < 0.01.

LC3 fluorescent protein aggregation was found between the pM and 3-MA groups, and significantly higher levels of LC3 expression and aggregation were observed in the cells belonging to the CQ and MgB groups. LC3 expression in the MgB group was significantly reduced after the addition of the autophagy inhibitor 3-MA, whereas LC3 aggregation was enhanced after the addition of CQ (Supplementary 3E). The same trends were also observed in TEM images (Fig. 6B, Supplementary 3D). The addition of 3-MA to the MgB group decreased the number of autophagic vesicles. The autophagic fluxes shown in Fig. 6C demonstrate that 3-MA could inhibit the formation of autophagosomes and autophagolysosomes. The number of autophagosomes increased after the addition of CQ (Supplementary 3F). As shown in Fig. 6D, no difference in the level of apoptosis was found between the pM, 3-MA, and CQ groups, but the apoptosis rates were significantly increased in the MgB group and significantly decreased after addition of the autophagy inhibitors 3-MA and CQ.

3.7. The AMPK/mTOR/ULK-1 pathway was involved in autophagy-dependent apoptosis induced by the Mg-coated Ti6Al4V scaffolds

Western blot analysis of autophagy-related proteins showed that the MgA and MgB groups presented significantly higher levels of phosphorylated AMPK and ULK-1 and significantly lower levels of phosphorylated mTOR than the pM and Ti groups, as shown by greyscale analysis (Fig. 7A). The addition of compound C, an AMPK inhibitor, to the MgB group restored the phosphorylated mTOR and ULK-1 levels (Fig. 7B). LC3 fluorescence staining showed that the addition of compound C significantly reduced the expression of LC3 in 143B and HOS cells belonging to the MgB group (Fig. 7C, Supplementary 3G).

3.8. In vivo verification of the anti-OS effects of the biofunctional Mg-coated Ti6Al4V scaffolds

The tumor volume growth curves are shown in Fig. 8A. The MgA and MgB groups presented slower tumor growth compared with the control and Ti groups. The tumor volumes in the different groups after 30 days are shown in Fig. 8B. The average tumor volumes in the Ti group were lower than those in the control group, but the difference was not significant. The average tumor volumes in the MgA and MgB groups were significantly lower than those in the control and Ti groups ($p < 0.01$). Autophagy-related and apoptosis-related markers were investigated by IF and TUNEL staining, and the results are shown in Fig. 8C. More TUNEL-positive cells were observed in the MgA and MgB groups than in the control and Ti groups, and

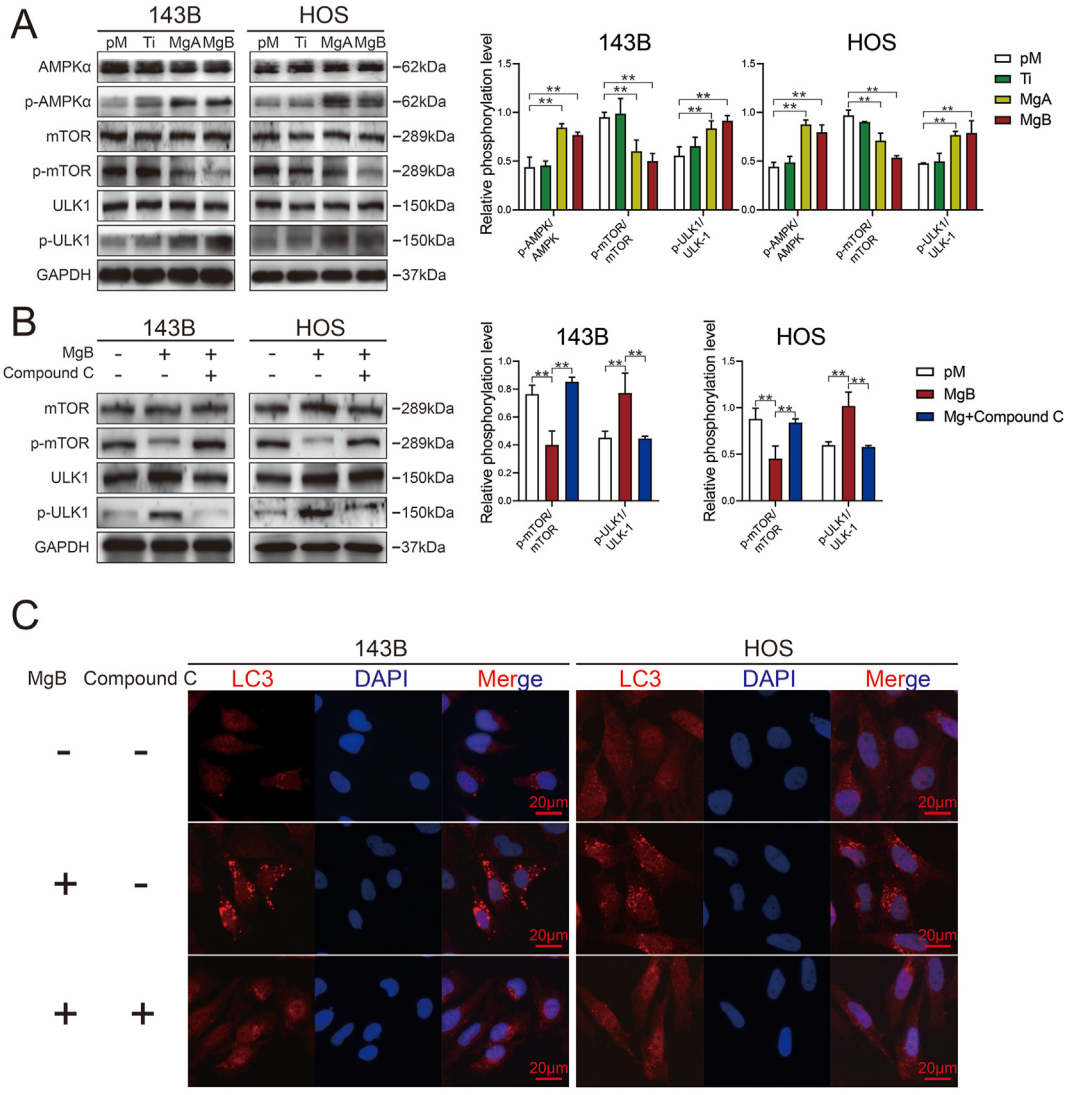

Fig. 7. The Mg-coated Ti6Al4V scaffolds induced autophagy-dependent apoptosis in 143B and HOS cells through the AMPK/mTOR/ULK1 signaling pathway. **(A)** Western blot analysis of phosphorylated AMPK, mTOR, and ULK1 in response to different treatments. **(B)** Western blot analysis of phosphorylated mTOR and ULK1 in the MgB group after treatment with compound C. The relative phosphorylated protein expression level was quantified. n = 3; **p < 0.01. **(C)** LC3 puncta formation in the MgB group with or without AMPK inhibition.

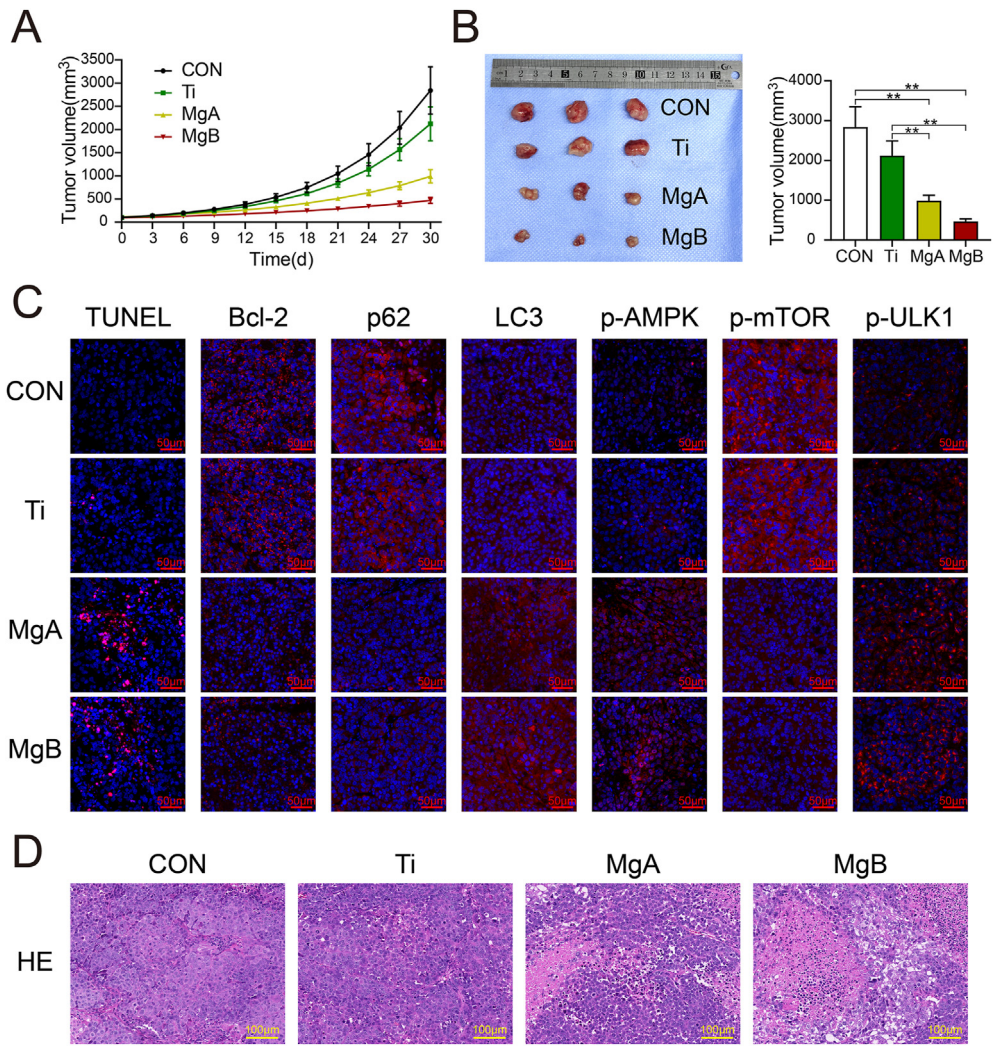

Fig. 8. Anti-OS effects of the Mg-coated Ti6Al4V scaffolds *in vivo*. (**A**) Tumor growth in tumor-bearing mice treated with different extracts. (**B**) Images and calculated volumes of harvested tumors after 30 days. n = 3; **p < 0.01. (**C**) TUNEL staining (apoptotic cells shown in red) and histological IF staining of Bcl-2, p62, LC3, p-AMPK, p-mTOR, and p-ULK1 in tumor sections (red indicates positive expression; the nuclei were stained blue by DAPI). (**D**) HE staining of tumor tissues.

the results from a histological IF analysis showed that the expression of the Bcl-2 protein, which inhibits apoptosis, was significantly decreased in the former groups. The expression of LC3 was upregulated, and the expression of the p62 protein was decreased, which indicated enhanced autophagy in tumors. Furthermore, the expression of p-AMPKα and p-ULK1 was increased, and the expression of phosphorylated mTOR was decreased, which suggested that the *in vivo* mechanism of tumor inhibition was consistent with the *in vitro* results. Histopathology images of tumor tissues obtained by HE staining are shown in Fig. 8D. The OS cells in the control and Ti groups were tightly arranged and showed deep-blue staining and vigorous growth. In the MgA and MgB groups, a large area of necrotic tumor cells with red staining was observed, and the remaining tumor cells in the adjacent necrotic area were loosely arranged and showed dissolved nuclei and inconspicuous cytoplasmic staining.

4. Discussion

As a classic type of orthopedic implant, Ti6Al4V prostheses are widely used for the treatment of large bone defects. Although many other titanium alloys, such as Ti–Nb alloys [33], exhibit excellent mechanical properties and biocompatibility, Ti6Al4V remains indispensable for clinical applications and bone tissue engineering [34]. In recent years, porous Ti6Al4V scaffolds have attracted more attention due to their low overall modulus of elasticity, excellent mechanical properties, and good ingrowth of new bone [35]. However, the excellent postoperative recovery achieved by the use of Ti6Al4V prostheses for reconstruction after OS resection can be easily eliminated by the local recurrence of OS. Therefore, the development of functional anti-OS materials is needed. Implants composed of Ti6Al4V do not show this property due to their low bioactivity. Ions and microfragments released during biological corrosion may even increase the risk of recurrence [5,6]. Therefore, the integration of anti-OS activity into Ti6Al4V scaffolds is crucial for their clinical application in limb salvage therapy.

Surface modifications with antitumor coatings are important strategies for optimizing Ti6Al4V scaffolds. A coating with antitumor drugs, such as doxorubicin, PD-L1, and other targeted drugs, has been found to be effective [36–38]. Unfortunately, due to the surface inertness of titanium alloys, the direct binding of drugs on their surface is difficult. Although pretreatments, such as dopamine coating, can bind the drug on the surface of the material, shortcomings such as a low dose-loading capacity and poor drug release have also been observed, which makes clinical application difficult. In contrast, the application of metallic coatings, such as Zn, Gu, Ni, and Ag, to Ti6Al4V surfaces is markedly easier [39–41]. In our research, the surface of Ti6Al4V scaffolds was successfully coated with Mg [20,21]. Mg, an excellent biodegradable and bioactive metal, can perform multiple biological functions through Mg^{2+} ion release during degradation [42]. In recent years, the tumor-inhibiting

effects of Mg have received extensive attention. Yangmei Chen et al. confirmed that Mg metal could inhibit breast carcinoma *in vivo* [12]. Shuang Qiao et al. reported that Mg wires could suppress the growth of ovarian tumors and promote apoptosis [13]. Some studies have also revealed that Mg and its alloys exert excellent inhibitory effects on the proliferation and metastasis of OS [43]. Mei Li et al. found that Mg could strongly inhibit cell adherence, affect cell morphology and decrease the number of MG-63 cells [14]. Rui Zan et al. found that excessive Mg^{2+} and reactive oxygen species (ROS) released during the degradation of Mg wires could effectively inhibit the growth of OS and prolong the survival of OS-bearing mice [44]. Although these studies have revealed the antitumor effects of Mg metal, the specific mechanisms have not been fully revealed, and the inhibitory effects of Mg^{2+} on OS need exploration. In this study, we further quantified the optimal concentration of Mg^{2+} with respect to activity against OS. We noted that the OS-suppressive effects of Mg^{2+} were enhanced with increases in the Mg^{2+} concentration. However, Mg^{2+} ions at high concentrations can also be toxic to normal cells, including osteogenic cells and endothelial cells. Qin L et al. tested the toxic effects of biodegradable Mg on osteoblasts, MC3T3-E1 cells, bone marrow stem cells (BMSCs), and L929 cells and recommended 10–20 mM as the maximum Mg ion dose for sustaining a cell viability level higher than 75% [17]. As a result, we believe that relatively high concentrations (15–20 mM) of Mg^{2+} yield the most appropriate range of Mg^{2+} release to exert anti-OS activity.

Ideal prostheses for post-OS reconstruction should perform both supportive and biological functions, such as osteogenic, angiogenic, and antirecurrence activities [45]. Mg metal, which is multifunctional and degradable, is thus a potential candidate. However, rapid and nonuniform corrosion has been the major factor restricting the use of pure Mg as a support material [46]. To take full advantage of the bioactive nature of Mg metal and the mechanical properties of Ti alloy, we designed and manufactured biofunctional Mg-coated porous Ti6Al4V scaffolds in an attempt to meet the needs of post-OS reconstruction. In previous studies, we found that functional scaffolds have favorable osteogenic and angiogenic properties, which are beneficial to the rapid recovery of the patient's limb function after surgery [20]. However, for patients with OS, reducing tumor recurrence may be more important than restoring limb function. In this study, we found that biofunctional scaffolds could rapidly release Mg^{2+} ions to result in the accumulation of relatively high concentrations. Further experimental results demonstrated that the scaffolds could significantly inhibit the proliferation and migration of OS cells. Tumor cell apoptosis was also clearly activated by the scaffolds. These results suggested that the Mg-coated Ti6Al4V scaffolds can inhibit OS recurrence, and the mechanisms need to be investigated in depth.

Recent studies have shown that the combined occurrence of autophagy and apoptosis acts as an important factor for tumor recurrence [47]. Many studies have confirmed that autophagy induction can promote apoptosis in OS. Zhuochao Liu et al. reported that atezolizumab could induce mitochondrial-related apoptosis by targeting autophagy [23]. Zhen Pan et al. found that chitooligosaccharide exerts an antitumor effect against OS by triggering pro-apoptotic autophagy through the p53/mTOR signaling pathway [24]. In addition, the occurrence of autophagy is closely associated with cationic changes during human physiological activities [27]. However, the effects of Mg on autophagy in OS have rarely been reported. In this study, we found that the biofunctional Mg-coated Ti6Al4V scaffolds upregulated autophagy in apoptotic OS cells. The inhibition of autophagy alleviated the increase in apoptosis induced by the biofunctional scaffolds. Therefore, the biofunctional scaffolds most likely activated autophagy-dependent apoptosis through autophagy-related pathways and thereby inhibited OS cells.

Although the mechanisms of Mg-related antitumor activity have been widely investigated in recent years, the research remains inconclusive. Hydrogen generation, changes in pH, and Mg^{2+} ion release during degradation are all influential factors in this activity. A few studies have demonstrated that H_2 and OH^- release induced by Mg could inhibit tumor proliferation through free radical accumulation [12], and Mg^{2+} ion release could arrest tumor cells at the G0/G1 phase of the cell cycle [13]. However, the mechanism through which excessive Mg^{2+} ions outside the cell trigger this process was not investigated. As an essential element in organisms, Mg activates more than 300 enzymes [48]. Through ion channels such as TRPM7, extracellular Mg^{2+} ions can interact with intracellular divalent cations or α-kinase, which then phosphorylates downstream substrates and participates in cell functions, including differentiation, proliferation, migration, and apoptosis [49]. In our study, we found that Mg^{2+} ions released by the biofunctional scaffolds activated the phosphorylation of AMPK in OS cells. AMP-dependent protein kinase (AMPK) is related to energy metabolism and autophagy [50,51]. Our subsequent experiments showed that the AMPK/mTOR/-ULK1 pathway was involved in the upregulation of autophagy in OS cells induced by the biofunctional scaffolds. In summary, the Mg-coated biofunctional Ti6Al4V scaffolds induced autophagy-dependent apoptosis via the AMPK/mTOR/ULK1 pathway.

Consistent with the *in vitro* experiments, our *in vivo* experiments also indicated the anti-OS effects of the biofunctional scaffolds. Both short-term and long-term Mg release from the biofunctional scaffolds significantly inhibited the growth of OS, and the regulation of autophagy-dependent apoptosis observed *in vivo* was consistent with the *in vitro* experiments. Although unlike chemotherapy drugs and targeted drugs, multifunctional scaffolds lack the ability to control metastatic tumors, these scaffolds may reduce the local OS recurrence rate. Moreover, biofunctional scaffolds, which are simple but effective, can be easily manufactured and used for clinical transformation. Although it is beneficial for tumor suppression, the rapid release of Mg from the coating at the early stage may affect long-term vascular ingrowth and bone ingrowth. Thus, further studies should be performed, and the relationships among OS inhibition, angiogenesis, and osteogenesis should be carefully evaluated before clinical application.

5. Conclusions

For reducing the possibility of local recurrence after OS resection and reconstruction, a multifunctional Mg coating is an important surface modification strategy for widely used Ti6Al4V prostheses. In addition to their angiogenic and osteogenic properties, we found that the Mg-coated biofunctional Ti6Al4V scaffolds could significantly inhibit the proliferation and migration of 143B and HOS cells. Furthermore, we also demonstrated that Mg^{2+} released by the functional scaffolds might activate the AMPK/mTOR/ULK1 pathway and induce autophagy-dependent apoptosis in OS. As a continuation of our previous study, the current study explored the anti-OS potential of the Mg-coated biofunctional Ti6Al4V scaffolds, and additional exploration is needed for their further clinical application.

CRediT authorship contribution statement

Xinghui Wei: Conceptualization, Methodology, Formal analysis, Writing-original draft. **Zhen Tang:** Methodology Validation, Formal analysis. **Hao Wu:** Methodology, Investigation, Writing-original draft. **Xiaoshuang Zuo:** Methodology, Validation. **Hui Dong:** Formal analysis, Investigation, Visualization. **Lili Tan:** Resources, Investigation. **Wei Wang:** Formal analysis, Investigation. **Yichao Liu:** Resources, Methodology. **Zhigang Wu:** Resources, Data curation. **Lei Shi:** Investigation. **Ning Wang:** Formal analysis. **Xiaokang Li:** Conceptualization, Resources, Supervision. **Xin Xiao:** Writing - review and editing, Funding acquisition. **Zheng Guo:** Conceptualization, Methodology, Supervision, Writing-review and editing.

Declaration of competing interest

The authors declare that they have no known competing financial interests or personal relationships that could have appeared to influence the work reported in this paper.

Acknowledgements

This work was supported by grants from Key R&D program of Shaanxi Province (2020SF-075), the National Key Research and Development Program of China (grant number 2017YFC1104900), The National Natural Science Foundation of China (No.51871239, 51771227, 81902897 and 81772328) and Incubation Project of the Army's Medical Technology Youth Cultivation Program of China (17QNP021).

Appendix A. Supplementary data

Supplementary data to this article can be found online at https://doi.org/10.1016/j.mtbio.2021.100147.

References

[1] I. Gazouli, A. Kyriazoglou, I. Kotsantis, M. Anastasiou, A. Pantazopoulos, M. Prevezanou, I. Chatzidakis, G. Kavourakis, P. Economopoulou, V. Kontogeorgakos, P. Papagelopoulos, A. Psyrri, Systematic review of recurrent osteosarcoma systemic therapy, Cancers 13 (8) (2021) 1757, https://doi.org/10.3390/cancers13081757.

[2] L.M. Jeys, A. Kulkarni, R.J. Grimer, S.R. Carter, R.M. Tillman, A. Abudu, Endoprosthetic reconstruction for the treatment of musculoskeletal tumors of the appendicular skeleton and pelvis, JBJS 90 (6) (2008) 1265–1271, https://doi.org/10.2106/jbjs.F.01324.

[3] D.J. Harrison, D.S. Geller, J.D. Gill, V.O. Lewis, R. Gorlick, Current and future therapeutic approaches for osteosarcoma, Expet Rev. Anticancer Ther. 18 (1) (2018) 39–50, https://doi.org/10.1080/14737140.2018.1413939.

[4] D. Pushpam, V. Garg, S. Ganguly, B. Biswas, Management of refractory pediatric sarcoma: current challenges and future prospects, OncoTargets Ther. 13 (2020) 5093–5112, https://doi.org/10.2147/ott.S193363.

[5] V. Levašič, I. Milošev, V. Zadnik, Risk of cancer after primary total hip replacement: the influence of bearings, cementation and the material of the stem, Acta Orthop. 89 (2) (2018) 252, https://doi.org/10.1080/17453674.2018.1440456.

[6] J. Pajarinen, E. Jamsen, Y.T. Konttinen, S.B. Goodman, Innate immune reactions in septic and aseptic osteolysis around hip implants, J. Long Term Eff. Med. Implants 24 (4) (2014) 283–296, https://doi.org/10.1615/jlongtermeffmedimplants.2014010564.

[7] G.M. Keegan, I.D. Learmonth, C.P. Case, Orthopaedic metals and their potential toxicity in the arthroplasty patient: a review of current knowledge and future strategies, the Journal of bone and joint surgery, British Volume 89 (5) (2007) 567–573, https://doi.org/10.1302/0301-620x.89b5.18903.

[8] V. Herber, B. Okutan, G. Antonoglou, N.G. Sommer, M. Payer, Bioresorbable magnesium-based alloys as novel biomaterials in oral bone regeneration, General Rev. Clinical Perspectives 10 (9) (2021) 1842.

[9] M. Razavi, Y. Huang, Assessment of magnesium-based biomaterials: from bench to clinic, Biomaterials Sci. 7 (6) (2019) 2241–2263, https://doi.org/10.1039/c9bm00289h.

[10] M. Shahin, K. Munir, C. Wen, Y. Li, Magnesium matrix nanocomposites for orthopedic applications: a review from mechanical, corrosion, and biological perspectives, Acta Biomater. 96 (2019) 1–19, https://doi.org/10.1016/j.actbio.2019.06.007.

[11] T. Imwinkelried, S. Beck, B. Schaller, Pre-clinical testing of human size magnesium implants in miniature pigs: implant degradation and bone fracture healing at multiple implantation sites, Mater. Sci. Eng. C 108 (2020), https://doi.org/10.1016/j.msec.2019.110389.

[12] Y. Chen, M. Xiao, H. Zhao, B. Yang, On the antitumor properties of biomedical magnesium metal, J. Mater. Chem. B 3 (5) (2015) 849–858, https://doi.org/10.1039/C4TB01421A.

[13] S. Qiao, Y. Wang, R. Zan, H. Wu, Y. Sun, H. Peng, R. Zhang, Y. Song, J. Ni, S. Zhang, X. Zhang, Biodegradable Mg implants suppress the growth of ovarian tumor, ACS Biomater. Sci. Eng. 6 (3) (2020) 1755–1763, https://doi.org/10.1021/acsbiomaterials.9b01703.

[14] M. Li, L. Ren, L. Li, P. He, G. Lan, Y. Zhang, K. Yang, Cytotoxic effect on osteosarcoma MG-63 cells by degradation of magnesium, J. Mater. Sci. Technol. 30 (9) (2014) 888–893, https://doi.org/10.1016/j.jmst.2014.04.010.

[15] M. Li, M. Yao, W. Wang, P. Wan, X. Chu, Y. Zheng, K. Yang, Y. Zhang, Nitrogen-containing bisphosphonate-loaded micro-arc oxidation coating for biodegradable magnesium alloy pellets inhibits osteosarcoma through targeting of the mevalonate pathway, Acta Biomater. 121 (2021) 682–694, https://doi.org/10.1016/j.actbio.2020.11.019.

[16] Q. Wang, S. Jin, X. Lin, Y. Zhang, L. Ren, K. Yang, Cytotoxic effects of biodegradation of pure Mg and MAO-Mg on tumor cells of MG63 and KB, J. Mater. Sci. Technol. 30 (5) (2014) 487–492, https://doi.org/10.1016/j.jmst.2014.03.004.

[17] J. Wang, F. Witte, T. Xi, Y. Zheng, K. Yang, Y. Yang, D. Zhao, J. Meng, Y. Li, W. Li, K. Chan, L. Qin, Recommendation for modifying current cytotoxicity testing standards for biodegradable magnesium-based materials, Acta Biomater. 21 (2015) 237–249, https://doi.org/10.1016/j.actbio.2015.04.011.

[18] G.K. Meenashisundaram, N. Wang, S. Maskomani, S. Lu, S.K. Anantharajan, S.T. Dheen, S.M.L. Nai, J.Y.H. Fuh, J. Wei, Fabrication of Ti + Mg composites by three-dimensional printing of porous Ti and subsequent pressureless infiltration of biodegradable Mg, Mater. Sci. Eng. C Mater. Biol. Appl. 108 (2020) 110478, https://doi.org/10.1016/j.msec.2019.110478.

[19] S. Ouyang, Y. Liu, Q. Huang, Z. Gan, H. Tang, Effect of composition on in vitro degradability of Ti-Mg metal-metal composites, Mater. Sci. Eng. C Mater. Biol. Appl. 107 (2020) 110327, https://doi.org/10.1016/j.msec.2019.110327.

[20] P. Gao, B. Fan, X. Yu, W. Liu, J. Wu, L. Shi, D. Yang, L. Tan, P. Wan, Y. Hao, S. Li, W. Hou, K. Yang, X. Li, Z. Guo, Biofunctional magnesium coated Ti6Al4V scaffold enhances osteogenesis and angiogenesis in vitro and in vivo for orthopedic application, Bioactive Mater. 5 (3) (2020) 680–693, https://doi.org/10.1016/j.bioactmat.2020.04.019.

[21] X. Li, P. Gao, P. Wan, Y. Pei, L. Shi, B. Fan, C. Shen, X. Xiao, K. Yang, Z. Guo, Novel bio-functional magnesium coating on porous Ti6Al4V orthopaedic implants: in vitro and in vivo study, Sci. Rep. 7 (2017) 40755, https://doi.org/10.1038/srep40755.

[22] O. Camuzard, M.C. Trojani, S. Santucci-Darmanin, S. Pagnotta, V. Breuil, G.F. Carle, V. Pierrefite-Carle, Autophagy in osteosarcoma cancer stem cells is critical process which can Be targeted by the antipsychotic drug thioridazine, Cancers 12 (12) (2020), https://doi.org/10.3390/cancers12123675.

[23] Z. Liu, H. Wang, C. Hu, C. Wu, J. Wang, F. Hu, Y. Fu, J. Wen, W. Zhang, Targeting autophagy enhances atezolizumab-induced mitochondria-related apoptosis in osteosarcoma, Cell Death Dis. 12 (2) (2021) 164, https://doi.org/10.1038/s41419-021-03449-6.

[24] Z. Pan, D.D. Cheng, X.J. Wei, S.J. Li, H. Guo, Q.C. Yang, Chitooligosaccharides inhibit tumor progression and induce autophagy through the activation of the p53/mTOR pathway in osteosarcoma, Carbohydr. Polym. 258 (2021) 117596, https://doi.org/10.1016/j.carbpol.2020.117596.

[25] L.M. Schwartz, Autophagic cell death during development - ancient and mysterious, Front. Cell Dev. Biol. 9 (2021) 656370, https://doi.org/10.3389/fcell.2021.656370.

[26] D. Sun, W. Tao, F. Zhang, W. Shen, J. Tan, L. Li, Q. Meng, Y. Chen, Y. Yang, H. Cheng, Trifolirhizin induces autophagy-dependent apoptosis in colon cancer via AMPK/mTOR signaling, Signal Trans. Targeted Therapy 5 (1) (2020) 174, https://doi.org/10.1038/s41392-020-00281-w.

[27] S. Sahni, D.H. Bae, P.J. Jansson, D.R. Richardson, The mechanistic role of chemically diverse metal ions in the induction of autophagy, Pharmacol. Res. 119 (2017) 118–127, https://doi.org/10.1016/j.phrs.2017.01.009.

[28] M. Perez-Neut, L. Haar, V. Rao, S. Santha, K. Lansu, B. Rana, W.K. Jones, S. Gentile, Activation of hERG3 channel stimulates autophagy and promotes cellular senescence in melanoma, Oncotarget 7 (16) (2016) 21991–22004, https://doi.org/10.18632/oncotarget.7831.

[29] M. Gao, P. Monian, Q. Pan, W. Zhang, J. Xiang, X. Jiang, Ferroptosis is an autophagic cell death process, Cell Res. 26 (9) (2016) 1021–1032, https://doi.org/10.1038/cr.2016.95.

[30] D. Denoyer, S. Masaldan, S. La Fontaine, M.A. Cater, Targeting copper in cancer therapy: 'Copper that Cancer, Metall : Integrated Biometal Sci. 7 (11) (2015) 1459–1476, https://doi.org/10.1039/c5mt00149h.

[31] T. Miyazaki, T. Takenaka, T. Inoue, M. Sato, Y. Miyajima, M. Nodera, M. Hanyu, Y. Ohno, S. Shibazaki, H. Suzuki, Lipopolysaccharide-induced overproduction of nitric oxide and overexpression of iNOS and interleukin-1β proteins in zinc-deficient rats, Biol. Trace Elem. Res. 145 (3) (2012) 375–381, https://doi.org/10.1007/s12011-011-9197-4.

[32] T. Yu, F. Guo, Y. Yu, T. Sun, D. Ma, J. Han, Y. Qian, I. Kryczek, D. Sun, N. Nagarsheth, Y. Chen, H. Chen, J. Hong, W. Zou, J.Y. Fang, Fusobacterium nucleatum promotes chemoresistance to colorectal cancer by modulating autophagy, Cell 170 (3) (2017) 548–563.e16, https://doi.org/10.1016/j.cell.2017.07.008.

[33] R.V. Chernozem, M.A. Surmeneva, V.P. Ignatov, O.O. Peltek, A.A. Goncharenko, A.R. Muslimov, A.S. Timin, A.I. Tyurin, Y.F. Ivanov, C.R. Grandini, R.A. Surmenev, Comprehensive characterization of titania nanotubes fabricated on Ti-Nb alloys: surface topography, structure, physicomechanical behavior, and a cell culture assay, ACS Biomater. Sci. Eng. 6 (3) (2020) 1487–1499, https://doi.org/10.1021/acsbiomaterials.9b01857.

[34] E. Chudinova, A. Koptyug, Y. Mukhortova, A. Pryadko, A. Volkova, A. Ivanov, E. Plotnikov, Y. Khan, M. Epple, V. Sokolova, O. Prymak, T. Douglas, R. Surmenev, M. Surmeneva, Functionalization of additive-manufactured Ti6Al4V scaffolds with poly(allylamine hydrochloride)/poly(styrene sulfonate) bilayer microcapsule system containing dexamethasone, Mater. Chem. Phys. 273 (2021), https://doi.org/10.1016/j.matchemphys.2021.125099.

[35] W. Liu, X. Li, Y. Jiao, C. Wu, S. Guo, X. Xiao, X. Wei, J. Wu, P. Gao, N. Wang, Y. Lu, Z. Tang, Q. Zhao, J. Zhang, Y. Tang, L. Shi, Z. Guo, Biological effects of a three-dimensionally printed Ti6Al4V scaffold coated with piezoelectric BaTiO3 nanoparticles on bone formation, ACS Appl. Mater. Interfaces 12 (46) (2020) 51885–51903, https://doi.org/10.1021/acsami.0c10957.

[36] K. Zhang, Y. Bai, R. Xu, J. Li, F. Guan, The mechanism of PDA/PEI/5-Fu coated esophageal stent material on inhibiting cancer associated pathological cells, J. Biomed. Mater. Res. 108 (3) (2020) 814–821, https://doi.org/10.1002/jbm.a.36860.

[37] J. Liang, X. Jin, B. Chen, J. Hu, Q. Huang, J. Wan, Z. Hu, B. Wang, Doxorubicin-loaded pH-responsive nanoparticles coated with chlorin e6 for drug delivery and synergetic chemo-photodynamic therapy, Nanotechnology 31 (19) (2020) 195103, https://doi.org/10.1088/1361-6528/ab6fd5.

[38] X. Mu, M. Zhang, A. Wei, F. Yin, Y. Wang, K. Hu, J. Jiang, Doxorubicin and PD-L1 siRNA co-delivery with stem cell membrane-coated polydopamine nanoparticles for the targeted chemoimmunotherapy of PCa bone metastases, Nanoscale (2021), https://doi.org/10.1039/d0nr08024a.

[39] A. AlHazaa, I. Alhoweml, M.A. Shar, M. Hezam, H.S. Abdo, H. AlBrithen, Transient liquid phase bonding of Ti-6Al-4V and Mg-AZ31 alloys using Zn coatings, Materials 12 (5) (2019), https://doi.org/10.3390/ma12050769.
[40] J. Luo, N. Wang, L. Zhu, G. Wu, L. Li, M. Yang, L. Zhang, Y. Chen, Tribological properties of Ni/Cu/Ni coating on the Ti-6Al-4V alloy after annealing at various temperatures, Materials 13 (4) (2020), https://doi.org/10.3390/ma13040847.
[41] R.N. Salaie, A. Besinis, H. Le, C. Tredwin, R.D. Handy, The biocompatibility of silver and nanohydroxyapatite coatings on titanium dental implants with human primary osteoblast cells, Mater. Sci. Eng. C Mater. Biol. Appl. 107 (2020) 110210, https://doi.org/10.1016/j.msec.2019.110210.
[42] Y. Luo, C. Zhang, J. Wang, F. Liu, K.W. Chau, L. Qin, J. Wang, Clinical translation and challenges of biodegradable magnesium-based interference screws in ACL reconstruction, Bioactive Mater. 6 (10) (2021) 3231–3243, https://doi.org/10.1016/j.bioactmat.2021.02.032.
[43] Y. Dai, Y. Tang, X. Xu, Z. Luo, Y. Zhang, Z. Li, Z. Lin, S. Zhao, M. Zeng, B. Sun, L. Cheng, J. Zhu, Z. Xiong, H. Long, Y. Zhu, K. Yu, Evaluation of the mechanisms and effects of Mg-Ag-Y alloy on the tumor growth and metastasis of the MG63 osteosarcoma cell line, J. Biomed. Mater. Res. B Appl. Biomater. 107 (8) (2019) 2537–2548, https://doi.org/10.1002/jbm.b.34344.
[44] R. Zan, W. Ji, S. Qiao, H. Wu, W. Wang, T. Ji, B. Yang, S. Zhang, C. Luo, Y. Song, J. Ni, X. Zhang, Biodegradable magnesium implants: a potential scaffold for bone tumor patients, Sci. China Mater. 64 (2021) 1007, https://doi.org/10.1007/s40843-020-1509-2, 2095-8226.
[45] K.S. Mangat, L.M. Jeys, S.R. Carter, Latest developments in limb-salvage surgery in osteosarcoma, Expet Rev. Anticancer Ther. 11 (2) (2011) 205–215, https://doi.org/10.1586/era.10.225.
[46] F. Kiani, C. Wen, Y. Li, Prospects and strategies for magnesium alloys as biodegradable implants from crystalline to bulk metallic glasses and composites-A review, Acta Biomater. 103 (2020) 1–23, https://doi.org/10.1016/j.actbio.2019.12.023.
[47] C. Tam, S. Rao, M.M.Y. Waye, T.B. Ng, C.C. Wang, Autophagy signals orchestrate chemoresistance of gynecological cancers, Biochim. Biophys. Acta Rev. Canc 1875 (2) (2021) 188525, https://doi.org/10.1016/j.bbcan.2021.188525.
[48] G. An, Z. Du, X. Meng, T. Guo, R. Shang, J. Li, F. An, W. Li, C. Zhang, Association between low serum magnesium level and major adverse cardiac events in patients treated with drug-eluting stents for acute myocardial infarction, PLoS One 9 (6) (2014), https://doi.org/10.1371/journal.pone.0098971 e98971-e98971.
[49] Z.-G. Zou, F.J. Rios, A.C. Montezano, R.M. Touyz, TRPM7, magnesium, and signaling, Inter. J. Molecular Sci. 20 (8) (2019) 1877, https://doi.org/10.3390/ijms20081877.
[50] W.G. Aschenbach, K. Sakamoto, L.J. Goodyear, 5' adenosine monophosphate-activated protein kinase, metabolism and exercise, Sports Med. (Auckland, N.Z.) 34 (2) (2004) 91–103, https://doi.org/10.2165/00007256-200434020-00003.
[51] S. Alers, A.S. Löffler, S. Wesselborg, B. Stork, Role of AMPK-mTOR-Ulk1/2 in the regulation of autophagy: cross talk, shortcuts, and feedbacks, Mol. Cell Biol. 32 (1) (2012) 2–11, https://doi.org/10.1128/mcb.06159-11.